



## PAPER

## RECEIVED

25 June 2019

## REVISED

22 February 2020

## ACCEPTED FOR PUBLICATION

26 February 2020

## PUBLISHED

17 April 2020

# The effects of a transverse magnetic field on the dose enhancement of nanoparticles in a proton beam: a Monte Carlo simulation

Mohammadreza Parishan<sup>1</sup>, Reza Faghihi<sup>1,2</sup>, Noriyuki Kadoya<sup>3</sup> and Keiichi Jingu<sup>3</sup><sup>1</sup> Department of Nuclear Engineering, School of Mechanical Engineering, Shiraz University, Shiraz, Iran<sup>2</sup> Radiation Research Center, Shiraz University, Shiraz, Iran<sup>3</sup> Department of Radiation Oncology, Tohoku University Graduate School of Medicine, Sendai, JapanE-mail: [faghihir@shirazu.ac.ir](mailto:faghihir@shirazu.ac.ir)**Keywords:** nanoparticle, dose enhancement, magnetic field, proton therapy

## Abstract

High-Z nanoparticles (NP) as radio-sensitization agents provide the feasibility of dose localization within the tumor in radiotherapy. Dose enhancement of NPs in the presence of a magnetic field (MF) could be challenged when magnetic resonance imaging (MRI) systems are used as an image-guided system. The MF can influence dose enhancement of NPs at their interfaces and surrounding medium and affect their dose deposition behavior.

In the TOPAS Monte Carlo code, gold nanoparticle (GNP) and superparamagnetic iron oxide nanoparticle (SPION) were irradiated using 70 and 150 MeV proton beams, in presence of transverse MF strengths with 0, 1, 3, and 7 T. The changes in the liberated secondary electrons from NPs and their dose enhancement ratio (DER), magnetic dose enhancement ratio (MDER), and angular dose distribution in 10 nm shell thicknesses up to 500 nanometers from their centers were measured. The central plane of NPs was considered as a scorer. Its thickness was 2 nm and divided into 6-degree sectors with 10 nm radial length. The dose deposition in this voxelated scorer was calculated.

The values of the deposited doses around NPs decrease rapidly while the DERs resulted from the secondary electrons are increased. MDERs are changed within  $\pm 5\%$  and  $\pm 7\%$  for 20 and 50 nm radius NPs, respectively. The variation in the angular dose distribution around a singular NP was not considerable when different MF strengths were applied. The dose values in the voxelated central plane show very similar results for the same NPs types in the different MF strengths.

The typically used MF in the MRI systems would not considerably affect the energy deposition behavior of the secondary electrons produced in the interaction of proton beam with NPs, at least in the near vicinity of NPs. The DERs of NPs in a water medium resulted from emerged secondary electrons, experience a low degree of perturbation in the presence of an MF. The results of this study show that the NPs as dose enhancement agents can also be used in an MF without pronounced modification in their efficacy.

## 1. Introduction

Radiation therapy using the proton beam is one of the most promising approaches for cancer treatment. One of the most important advantages of the proton beam is that the Bragg peak occurs at a nearly precise depth that delivers a localized radiation dosage to the volume of the target and spares healthy tissues. Progress in nanotechnology has paved the way for a new strategy to enhance radiotherapy efficacy. The accumulation of high atomic number NP in the tumor can potentially increase the local dose of radiation (Bug *et al* 2010, Kirkby and Ghasroddashti 2015, McMahon *et al* 2016). The low energy secondary electrons generated through proton interaction with nanoparticles increase the physical dose in a small volume around the nanoparticles (Lin *et al* 2014, Wälzlein *et al* 2014, Ahmad *et al* 2016b, Her *et al* 2017).

Studies show that radio-enhancement by NP agents activated by ion beam and ionizing radiation begins in the cytoplasm, but considering the ranges of secondary liberated electrons, there is little chance to create damage to the DNA (Usami *et al* 2008, Lacombe *et al* 2017, Sotiropoulos *et al* 2017). However, there is not an obvious mechanism for cell death. Some hypotheses such as the increased generation of intracellular reactive oxygen species, increased apoptosis or direct DNA double-strand break have been put forward (De Jong *et al* 2008, Popovtzer *et al* 2016, Uz *et al* 2016). In this research, we suppose that the localized dose enhancement by the secondary electron that emerged from NPs is the main reason for the following radiobiological events. At present, using NP dose enhancement in the proton therapy is far from clinical trial and more studies on the different physical and biological aspects are necessary.

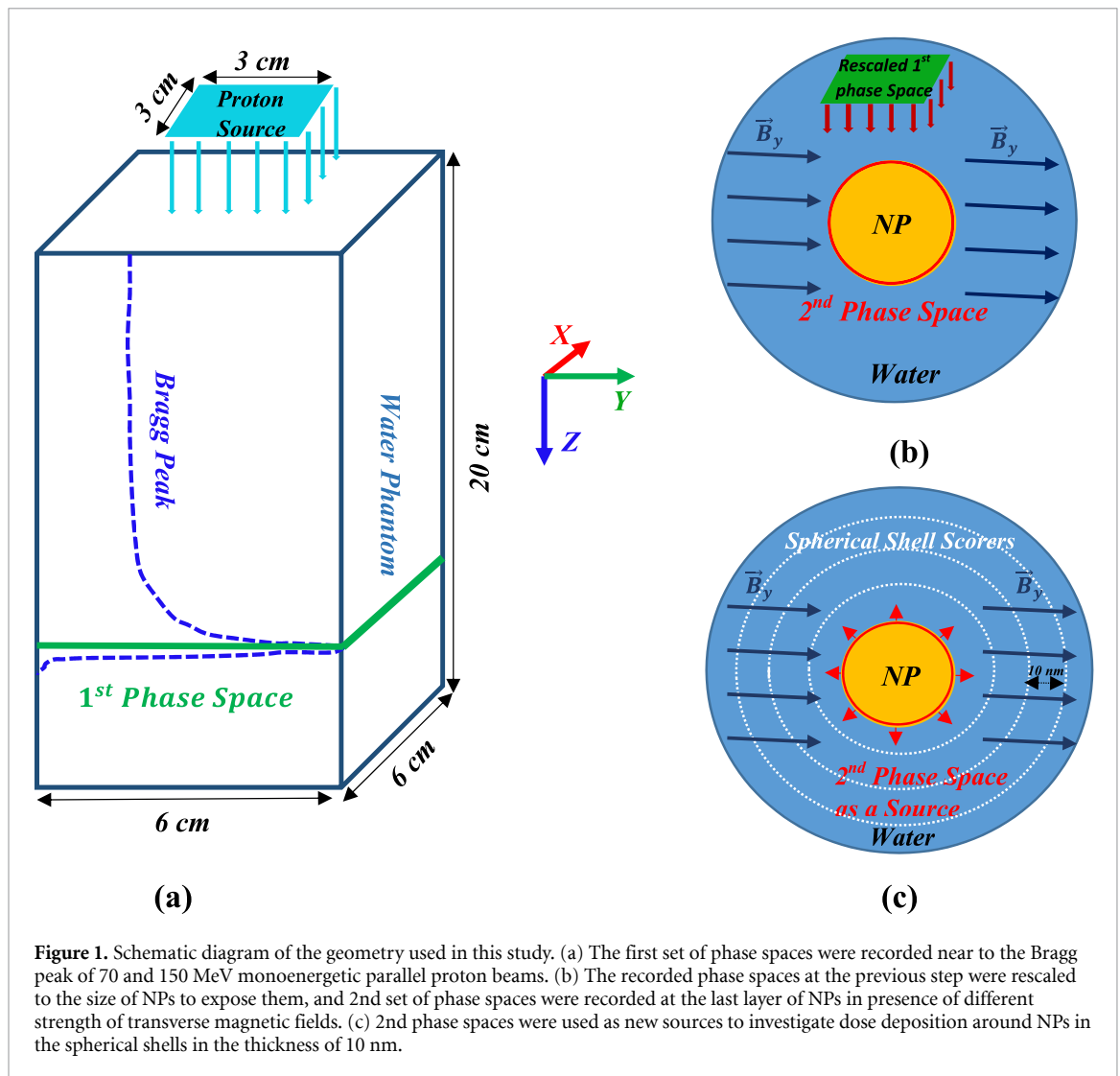
In recent years, the integration of the MRI as an image-guided device with dose delivery machines in radiotherapy has been attracted by significant studies. MRI-guided proton therapy (PT) as the next generation of image-guided proton therapy (IGPT) has benefits such as better soft-tissue contrast, real-time motion tracking, omitting imaging dose, etc (Ashburner 2009, Paganelli *et al* 2018, Stemkens *et al* 2018, 2019). However, the MR-guided PT is still in its infancy, and further researches on the different aspects of this hybrid system will be necessary to introduce it clinically.

The presence of electromagnetic interaction between dose delivery and MRI systems imposes several problems that should be studied before introducing the system clinically. The presence of the MF of the MRI system will lead to charge particles influence by the Lorentz force driven effect. Therefore, the change in the trajectory of them causes different results in dose distribution compared with the absence of the MF. The MF of MRI scanner can affect the trajectory of primary and secondary charged particles resulting in deflection and lateral displacement of the Bragg peak position (Raaymakers *et al* 2008, Moteabbed *et al* 2014, Fuchs *et al* 2017, Schellhammer *et al* 2018). Also, the effect of MF is especially pronounced for the interface of mediums with significant differences in mass density and atomic number (high and low). In the presence of an MF, the path of an electron will be bent and follow a helical form for which the radius ( $R$ ) can be calculated as the following formula (Chu *et al* 2000):

$$R = \frac{v_{\perp} m_0}{eB} \left( 1 + \frac{E}{E_0} \right); E_0 = m_0 c^2 \quad (1)$$

Where  $v_{\perp}$  is the electron velocity perpendicular to MF strength  $B$ ,  $c$  is the speed of light in the vacuum,  $m_0$  the rest mass,  $e$  the electrical charge, and  $E$  the energy of the electron. This equation shows that the radius of the helical trajectory decreases in higher MFs and lower energy of the electron. In a material with higher mass density and atomic number, the mean free path length of the electron is shorter in comparison with the radius of the helix. Therefore, the electrons experience many interactions with a bent trajectory between them (Raaymakers *et al* 2008, Raaijmakers *et al* 2008). However, in a material with a lower atomic number and mass density, the mean free path length in comparison to helix radius will be increased and the electron with a minimum number of interactions will go through a helical trajectory (Boye *et al* 2013). If this phenomenon occurs in the interfaces of two materials, the electron returns most of its energy to the origin emerged material and causes dose enhancement in the interface. Another point is the reduction of the number of electrons that deposited all of their energy in the second medium as well as the degradation of their effective ranges. The effect of MF of MRI on dose distribution was well studied by different investigators and various parameters were also considered (Moteabbed *et al* 2014, Schellhammer *et al* 2018). In most of these studies, the variation of the dose maps near the interface of soft tissue with air cavities, and also high-density tissues with soft tissues are significant (Ahmad *et al* 2016a).

The extracted electrons spectrum that emerges from an NP, indicates that many electrons have low energies in the order of a few keV or less, where their path lengths are on the sub-micron scale in a water-equivalent media. We also know that after each electron interaction with the matter, the electron energy decreases continuously. If we assume a static magnetic field with a given value, the decrease of the electron energy results in the reduction of the gyration radius. Therefore, the radius of rotation at the end of the electron path will be smaller than at the beginning of the motion. So, there is a chance for the low energy electrons to return to the NPs or at least alter their trajectories. On the other hand, Stochastic elements in the interaction of an electron with matter such as the scattering angle at the inelastic scattering with an orbital electron and the deflection by the elastic scattering with a nucleus lead to the nonlinearity of its path (Nikjoo *et al* 2012). So, after a collision, the direction of electron movement relative to the magnetic field direction is randomly distributed. Although the cumulative behavior of an electron beam is predictable on a macroscopic scale, on a microscopic and nanoscopic scale, the behavior of isotropically liberated electrons is more complicated in the presence of a magnetic field, especially in a denser matter than air. In the air, the number of interactions is very low and the path of the electron is more predictable. Small changes in the behavior of the electrons in a magnetic field may introduce significant differences in the dose enhancement



factors over a few hundred nm from the surface of NPs. Although the result of this research may be obvious and natural at first glance, all these doubts around the electron interaction on a nanoscopic scale in a magnetic field lead to some uncertainties in the final answer. We tried to answer this probable question.

In this study, for the first time, we try to explore to what extent an MRI static magnetic field influences the function of an NP as a dose enhancement agent in proton therapy. Our focus is on the DER caused by secondary particles liberated from NPs in a magnetic field. Magnetic dose enhancement ratio as a new factor was introduced to investigate the effect of different magnetic field strengths on the dose enhancement ratio of NPs. Superparamagnetic iron oxide nanoparticle (SPION) that is used as a contrast agent in MRI, and gold nanoparticle were chosen as two case studies. Different strengths of the MF, nanoparticle size, and proton energies were considered and dose deposition around nanoparticles was measured.

## 2. Material and methods

Monte Carlo simulation was done in the TOPAS version 3.1 (Perl *et al* 2012). This simulation was performed in three steps to reduce computation time (figure 1). While the Bragg peaks occur at the 4.0 and 15.7 cm depth of water for 70 and 150 MeV, the first phase spaces for primary proton beams were saved at the 4.0 and 14.6 cm depth of a water phantom with the dimension of  $6 \times 6 \times 20$  cm<sup>3</sup>, respectively (figure 1(a)). As can be seen in figure 2, the peak of the saved spectrum for the 150 MeV primary proton beam has a higher energy value compared to the 70 MeV proton beam. These phase spaces included all of the primary and secondary particles produced in the water medium.

On the second step, SPION (Fe<sub>3</sub>O<sub>4</sub>) and gold nanoparticle (GNP) were chosen as dose enhancement nanoparticles. SPION is a contrast agent in MRI and can increase the dose in Nanoscale sizes in radiation therapy, so it has the potential to be used as theranostic nanoparticle (Ahn *et al* 2018). GNP also has different

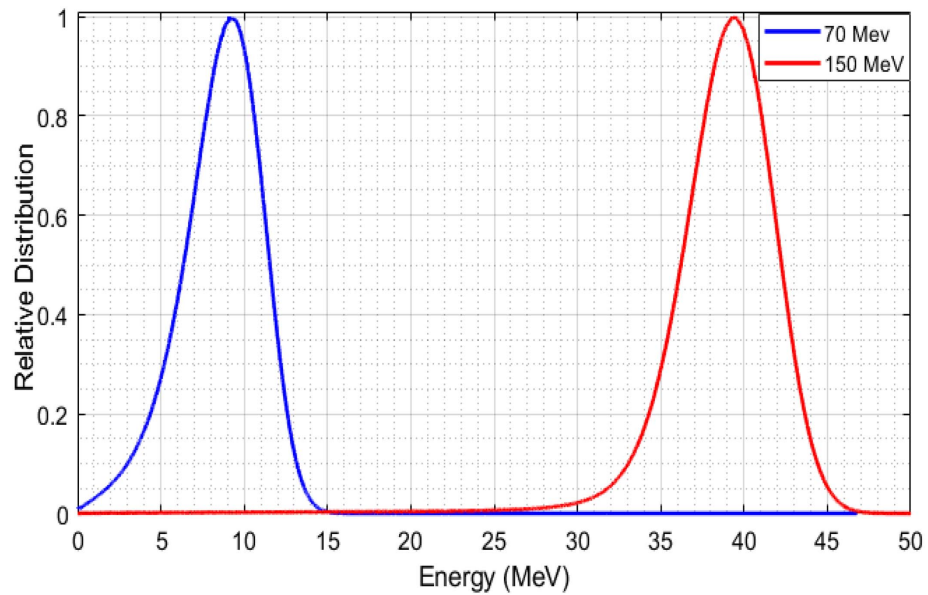


**Figure 2.** (a) Energy spectra of recorded proton particles near to the Bragg peak of the 70 and 150 MeV primary proton beams. The exact position of the Bragg peaks of 70 and 150 MeV proton beams are 4.0 and 15.7 cm, while the recorded phase spaces are in the 4.0 and 14.6 cm depth of water, respectively.

applications in cancer treatment and can increase the physical dose in a photon or ion beam therapy (Her *et al* 2017). Gold was selected as a material with high differences in the density and atomic number,  $Z$ , compared to water, and SPION as a dose enhancement material that is closer to the water in  $Z$  and density compared to gold. The effective atomic number and density of a SPION are 23.23 and  $5.17 \text{ g cm}^{-3}$ , respectively. These values for a gold nanoparticle are 79 and  $19.3 \text{ g cm}^{-3}$ , respectively. Water nanoparticle (WNP; Note that, W is not a symbol for tungsten) was defined to compare the results of GNP and SPION with a water medium without any nanoparticle. These three nanoparticles were considered in a spherical volume shape with two different radii of 20 nm and 50 nm. WNP has the same geometry as the other two NPs but its material is water, and thus provides a uniform medium with the surrounding medium.

SPIONs have a single magnetic domain and behave like a single magnetic dipole. The equation below can be used to determine the magnetic field produced by a single SPION with spherical symmetry in an applied MF in the  $Y$ -direction (Ortega and Giorgio 2012);

$$\vec{B} = \frac{\mu_0 m_d}{4\pi r^3} (3\cos\theta\sin\theta\hat{x} + (2 - 3\sin^2\theta)\hat{y}) \quad (2)$$

where  $\mu_0$  is the permeability of free space in SI units ( $4\pi \times 10^{-7} \text{ N/A}^2$ ),  $m_d$  is the magnetic dipole moment,  $r$  is the radial distance from the particle and  $\theta$  is the angle away from the magnetization vector. The magnetic field strength decreases proportionally to  $\frac{1}{r^3}$ . For example, at a distance of 8.3 nm from the surface of a 5 nm diameter SPION the magnetic field strength decreases to 0.01% of its maximum. So, the magnetization of a SPION has no significant effect on the uniformity of the applied magnetic field. We assumed that inside an NP the MF is uniform.

The magnetic properties of GNP have been studied by several groups, but the results are contradictory, so an obvious understanding of GNP magnetic properties is still missing (Agrachev *et al* 2017). If we neglect interparticle interaction, the ensemble-averaged response is paramagnetic (Gómez Vilorio *et al* 2018). To investigate the variation of the MF inside and outside of NP, we assumed exaggerated conditions. Four combinations of 0 and 7 tesla MF strengths were defined for inside and outside of NPs (GNP and SPION). The differences between numbers and spectra of liberated electrons from the same NPs were less than .001%. So, the definition of a uniform magnetic field inside and outside of the NPs is acceptable.

The extracted phase spaces at the first step were set as the new sources at a distance of 30 nm above the NPs to irradiate them (figure 1(b)). To increase the probability of interaction of the projectile particles with NP, the phase spaces were rescaled to a planar source with the dimension similar to the radius of the NP. In this way, nearly all of the projectile particles interact with NP, except for the particle with high angular emission, which caused a reduction of the computing time. The probability of interaction between projectile protons and NPs is too low, so we should consider a high number of primary histories that is not realistic in a clinical situation, but it is necessary to consider these high number of particles to obtain results with low

uncertainty. The final parameter for the decision should be DER, not the absolute value of the dose. The number of histories from the second phase space was set to  $3 \times 10^9$  particles. In this step, g4h-phy\_QGSP\_BIC\_HP and g4h-elastic\_HP were used as the physics model for proton interactions and Livermore and g4-DNA (opt2) for electromagnetic interaction in the NPs and water, respectively. The cut off length for all of the particles was set to 1 nm. All the options for the contribution of photoelectrons, Auger electrons, Fluorescence, and particle-induced x-ray emissions (PIXEs) were activated in the simulation procedure.

To investigate the effects of the MF on the number and dose deposition of secondary electrons emerged from NPs, the transverse dipole magnet fields in *Y*-direction with four strength values of 0, 1, 3, and 7 T were assigned to the water box including NPs. The equations of particle motion in a pure MF are solved utilizing Runge Kutta methods in Geant4 (GEANT4-Collaboration 2019). Both the minimum step and delta chord values were set to 1 nm.

To manage the time and uncertainty of simulation efficiently, a new phase space was considered on the outer layer of NPs in a thickness of 0.01 nm to record just second-generation particles emerging and going out from them (figure 1(c)). In this step, the dose deposition from secondary particles liberated from NPs was scored in the water medium to a distance of 150 nm from the center of the NPs in one bin.

On the last step, phase spaces recorded at the outer layer of NPs were used as a source to measure dose distribution around nanoparticles. The number of primary histories in this stage was considered as 25 000 000 particles. The dose was recorded in spherical shells of 10 nm thickness from the surface of NPs to a distance of 150 nm with 13 and 10 radial bins for 20 and 50 nm radius NPs, respectively. The dose was also recorded from 150 nm to 500 nm radial distance as one bin. Change in the angular distribution of secondary electrons around NPs was studied using scored dose in an angularly segmented cylindrical volume. Physical models and MF arrangements were added similarly to the last step. In most of the literature, in the definition of DER, the total deposited dose from various particles is considered to calculate dose in the water medium. In the present work, we aimed to focus only on the secondary electrons liberated from NPs, so DER was defined as,

$$DER = \frac{\text{Dose in water deposited by the liberated secondary from electron GNP or SPION}}{\text{Dose in water deposited by the liberated secondary from electron assumed WNP}} \quad (3)$$

Where just the deposited energy of the liberated secondary electrons from NPs was considered in the dose calculation. To investigate the role of an MF directly on the dose around a specific NP, MDER values were determined using the following equation:

$$MDER = \frac{DER \text{ at any magnetic field strength}}{DER \text{ without magnetic field}}. \quad (4)$$

### 3. Results and discussion

The energy spectrum of recorded proton particles at the Bragg peaks of 70 and 150 MeV primary proton beams is shown in figure 2. In this figure, just proton spectrums are shown while all of the secondary produced particles were recorded in the first phase space and considered in the next step interaction with NPs. In these two curves, the energy spectrum peaks are in the 9.2 and 39.3 MeV for 70 and 150 MeV, respectively. The first phase spaces for 70 and 150 MeV primary proton beams were saved at the 4.0 and 14.6 cm depth of water, respectively, while their Bragg peaks occur at the 4.0 and 15.7 cm depth of water. As can be seen in figure 2, the peak of the saved spectrum for the 150 MeV primary proton beam has a higher energy value compared to the 70 MeV proton beam. So, we had two separate proton energy spectra without any overlap that provide a situation in which NPs exposed with two completely different spectra. The spectra of beams with different primary energies have approximately the same energy distribution at their related Bragg peaks. But when distal layers of the target are scanned using the pencil beam scanning (PBS) method in proton therapy, some NPs which are distributed in the proximal layers of the target are exposed with proton particles that are not in the same energy as in their Bragg peak. So, we selected these two positions for the phase spaces to simulate a more realistic situation. The NPs that are exposed with phase space of 150 MeV primary beam are the same as NPs in the proximal layers when the beam is delivered to distal layers and phase space of the 70 MeV interact with NPs that are exactly distributed in the Bragg peak. Figure 3 shows the energy spectrum of the secondary electrons emerged from three types of NPs in the presence of a transverse MF and without it. Figure 3(a) compares the spectrum of secondary electrons in the 70 and 150 MeV proton beams. Figure 3(c) depicts the zoomed-in figure 3(a), for low energies. As shown in these figures, these curves reach their maximum at about 1 keV, and then start to decrease. The mean and



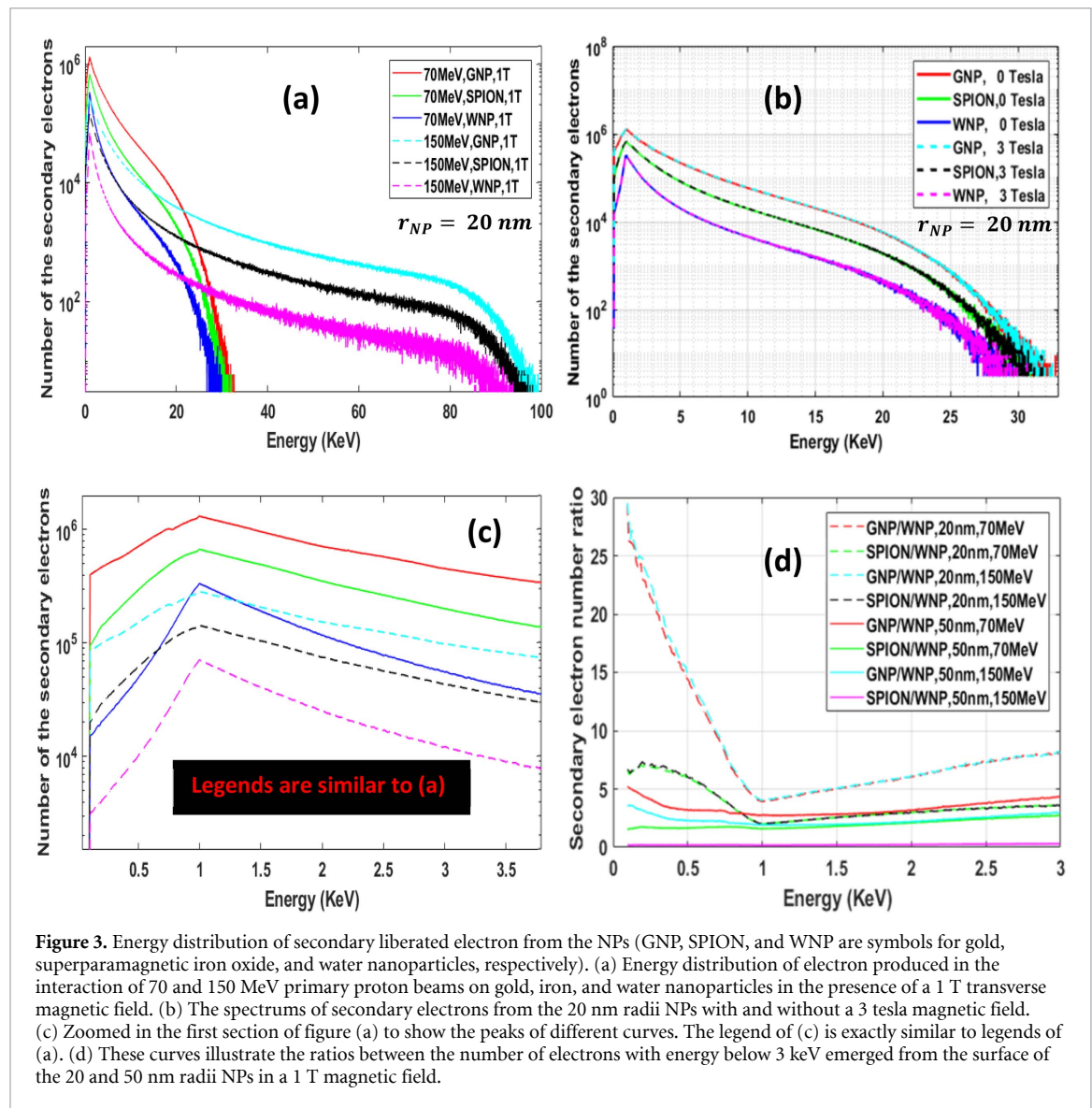


**Figure 3.** Energy distribution of secondary liberated electron from the NPs (GNP, SPION, and WNP are symbols for gold, superparamagnetic iron oxide, and water nanoparticles, respectively). (a) Energy distribution of electron produced in the interaction of 70 and 150 MeV primary proton beams on gold, iron, and water nanoparticles in the presence of a 1 T transverse magnetic field. (b) The spectrums of secondary electrons from the 20 nm radii NPs with and without a 3 tesla magnetic field. (c) Zoomed in the first section of figure (a) to show the peaks of different curves. The legend of (c) is exactly similar to legends of (a). (d) These curves illustrate the ratios between the number of electrons with energy below 3 keV emerged from the surface of the 20 and 50 nm radii NPs in a 1 T magnetic field.

maximum of the energy and the number of electrons liberated from the surface of GNP in both proton beams is higher than SPION and WNP. The higher number of electrons in gold NP is caused by higher mass density. The cross-sections for the production of the secondary electrons in a proton beam increase with the density of materials and decrease inversely with the square of the velocity of protons (Mckinnon *et al* 2016). The projectile primary protons with higher energies transfer more kinetic energy to the produced secondary electrons. These two reasons lead to the production of a larger number of electrons but with more limited ranges of energies in the 70 MeV beam compared to the 150 MeV beam.

As shown in figure 3(d) the ratio of the number of secondary electrons with energy lower than 3 keV emerged from GNP and SPION to WNP for 70 and 150 proton beams, and also 20 and 50 nm radii in a 1 T MF are illustrated. The maximum range of electron with 3 keV energy is about 500 nm in the water (Francis *et al* 2011). The curves for 20 nm radii NPs show a rapid decrease in their minimum at about 1 keV and then an increase. This behavior for 50 nm NPs is less significant. For these NPs, the secondary electron number ratio experiences a gradual decrease and then an increasing trend. As a description of the behavior of these curves, the first phase space was recorded from parallel particles, so the saved particles in the phase space had a near-uniform spatial distribution. The rescaled first phase space that was used as a source, irradiate NPs with an approximately uniform spatial flux of proton particles. So, the different parts of an NP do not experience the different flux of protons. On the other hand, a proton particle that traversed an NP from the regions near to its central chord instead of the peripheral chord, has a higher probability of interaction with NP, leading to a higher number of secondary electrons produced in the central region of NP. Many of these low energy electrons cannot reach the surface of the NP. The self-absorption of electrons inside NPs increase with their density and diameter, so many of these electrons do not have enough of a range to go out from NP

(Cho *et al* 2016, Mckinnon *et al* 2016). This behavior for GNP and 50 nm radius NP is more considerable in comparison with WNP.

For a 20 nm radius NP, the lower rate of self-absorption compared with the 50 nm one, causes a higher ratio of secondary electrons. However, in a 50 nm NP, the higher radius in comparison with the range of low energy electrons in gold and water causes a smooth decrease and increase of curves.

In figure 3(b), the effects of a 3 T MF on the spectrum of liberated electrons are shown. The figure implies there is not any significant difference between the spectra of electrons going out from NPs with or without MF. This result may have induced the thought of subsequent same dose deposition patterns around the NPs with and without MF. However, we should also consider the electron return effect for these secondary electrons as another possible phenomenon.

As the results of this study showed, it is unlikely to return a secondary electron to the nanoparticle itself. The secondary electrons undergo enough interactions in the soft tissue media (or simply water) around the high-density NP. The mean gyration radius over the entire electron path is large compared to the overall path length and therefore the electrons are locally absorbed before the Lorentz force significantly alters the trajectory. Also, the very small size of the nanoparticle means that even if the magnetic field is strong enough to influence the electron trajectory, the possibility to return to the same NP is very low.

Figures 4 and 5 show the dose deposited by the secondary electrons emerging from the 20 and 50 nm radii NPs, respectively. The dose distribution was measured by 10 nm thickness shells from the surface to 150 nm distance from their centers and was reported as the total dose deposited by all of the electrons normalized to the total number of primary protons in the run. Dose values decreased exponentially with distance from the surface of NPs. A large number of low energy secondary electrons from the GNP was followed by a greater dose value near this NP and also higher decay rate than the two others. This is similar to the results reported in previous studies (Tran *et al* 2016).

When NPs were irradiated in the 150 MeV proton beam, the total deposited dose was lower compared with 70 MeV. This happens because the mean energy of the proton particles recorded in the phase space of the 150 MeV beam is higher. The linear energy transfer of proton particles increases with decreasing the energy of primary protons which caused a higher number of generated secondary electrons in the 70 MeV beam and more deposited a nearer distance to the NPs (Tran *et al* 2016). When the MF strength increases to higher values, for both 20 and 50 nm particles, there is not any significant difference between the deposited dose around NPs. Dose enhancement ratios for NPs decrease up to a distance of about 50 nm and then increase to 8.3 and 5.0 values for 20 and 50 nm radii of the GNPs, respectively. Whereas such values for SPIONs are lower, about 3.7 and 2.7, respectively. When 20 nm NPs are irradiated in the 70 MeV beam, the gradient of DER curves is higher than in other cases.

The variations of the DER curves are smoother compared with the curves in figure 3(d), which showed the ratio of the number of the electrons with energy below 3 keV. The range of 3 keV electron is about 500 nm, and we limited the energy axis of figure 3(d) to this value. The range of 500 nm was considered because of the run time of our simulations. Adding any scorer with a higher number of divisions or voxels, and to further distances increases run times. It is worth noting that our cut ranges for particles are adjusted to nm order and this will increase the number of steps in the Monte Carlo simulations. So, we select this range for our simulation based on the performance of our systems for DERs calculations. It should be noted that the 100 nm or less than 300 nm distance is selected as the desired range of investigation in other related literature, and beyond this distance, the DER and number of electrons are not considerable (McMahon *et al* 2011a, 2011b, Wälzlein *et al* 2014, Cho *et al* 2016, Ahn *et al* 2017, 2018). These electrons (with energy less than 3 keV) constitute a high percentage of the electrons that deposit their energy in the near vicinity of the NPs. So, the ratio of these electrons that were liberated from the NPs could be an initial estimation of the ratio of deposited dose or DER to a 500 nm distance from the NPs.

One should keep in mind that in addition to the low energy electrons, more energetic electrons with higher ranges in the water media also have many interactions in shorter distances from the surface of the NPs, while they were not considered in figure 3(d). The higher number of electrons with energy more than 3 keV in the GNP and SPION compared with WNP, caused a deposition of more energy and finally higher dose values in the surrounding water media. As can be seen, the variations of the MF strength do not affect the DERs. As a consequence of this fact, it is obvious that a static MF cannot change the DERs around NPs, at least to a distance of about 150 nm from their centers. This are similar to another study on effects of an MF on dose distribution in a pure water medium (Raaymakers *et al* 2008). This study has shown that the dose absorbed distribution of secondary low-energy electrons produced by a therapeutic proton beam was unaltered in a static MF. The reason is that these secondary low-energy electrons will lose their energy before they experience a significant rotation in their path. This study has explained that electron return effect in proton therapy is negligible. It is worthy to note that the trajectory of primary proton is changed in the presence of a magnetic field, but the secondary electrons' behavior is approximately unchanged.

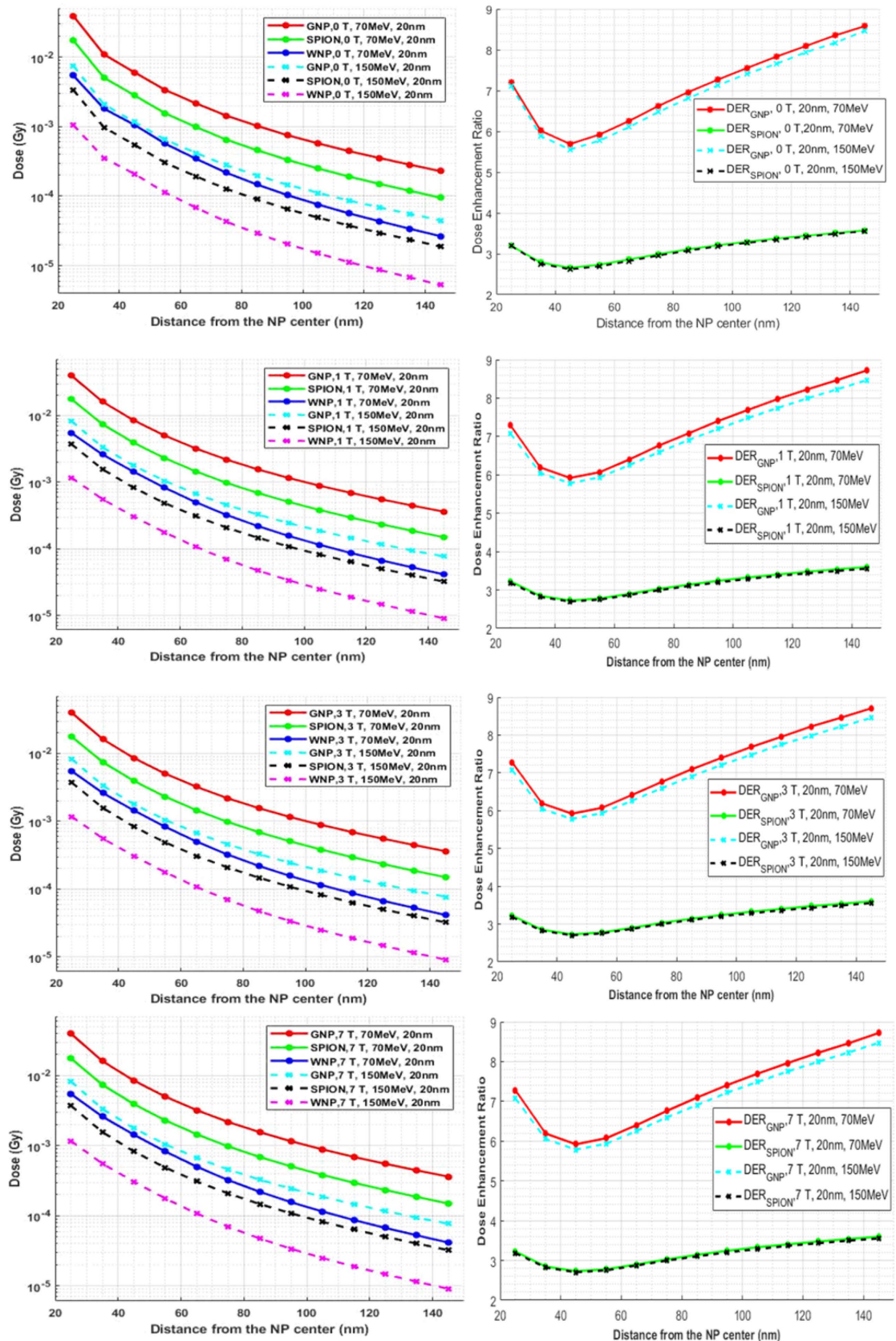


**Figure 4.** Left column: the dose distribution of the secondary electrons produced in interaction of 70 and 150 MeV primary proton beams with 20 nm radii NPs in different magnetic field strengths. Dose values were normalized to the total number of primary protons in the run. Right column: Dose enhancement ratios (DER) resulted from ratios of curves in their left figures.

MDER is defined as the DER of NP in any MF strength to its value without any MF (0 T). This parameter obligates the effects of WNP and directly compares the NPs with the same materials. For an NP in a given energy beam, this parameter does not change with MF strength, however, its variation with distance from the



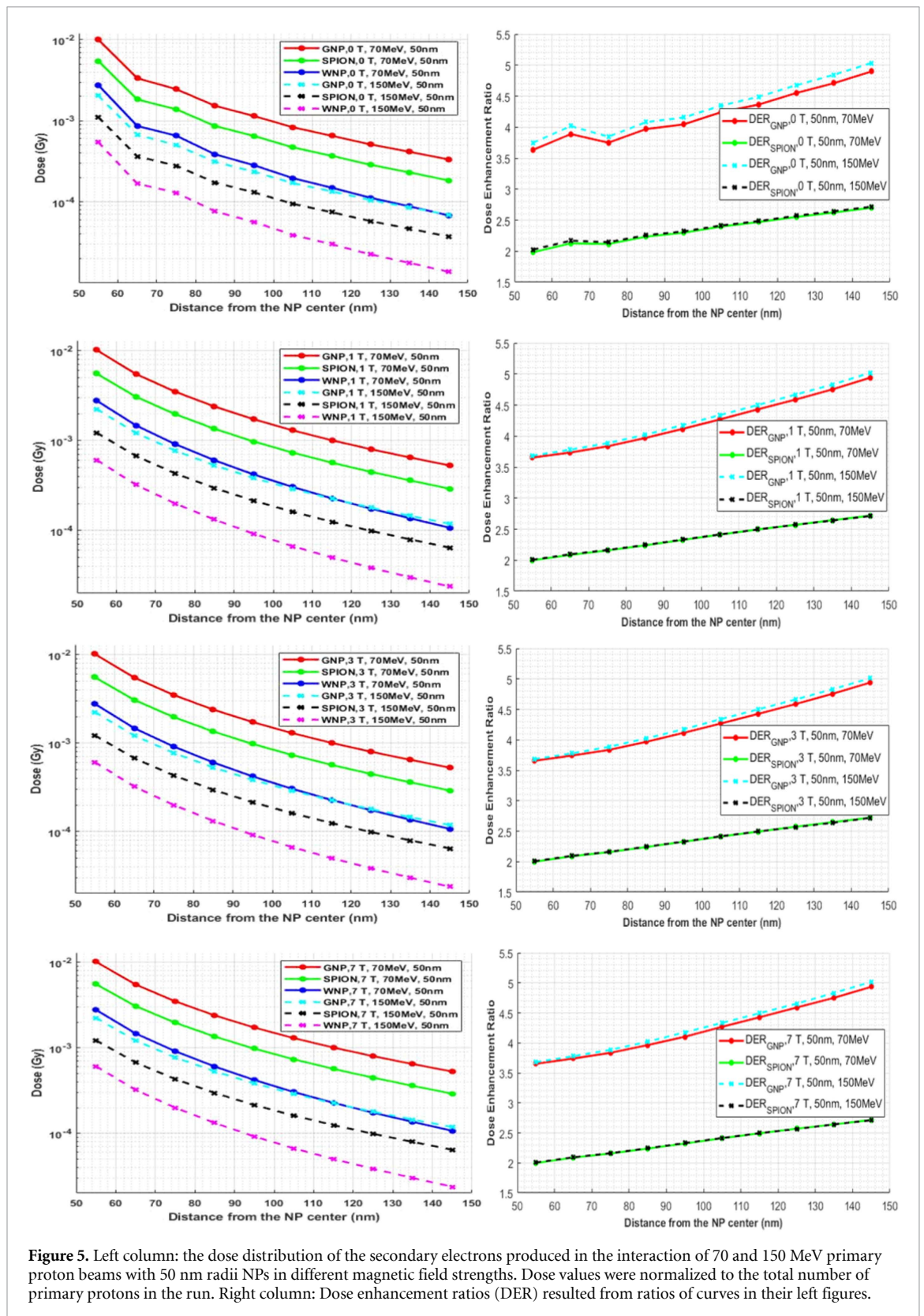
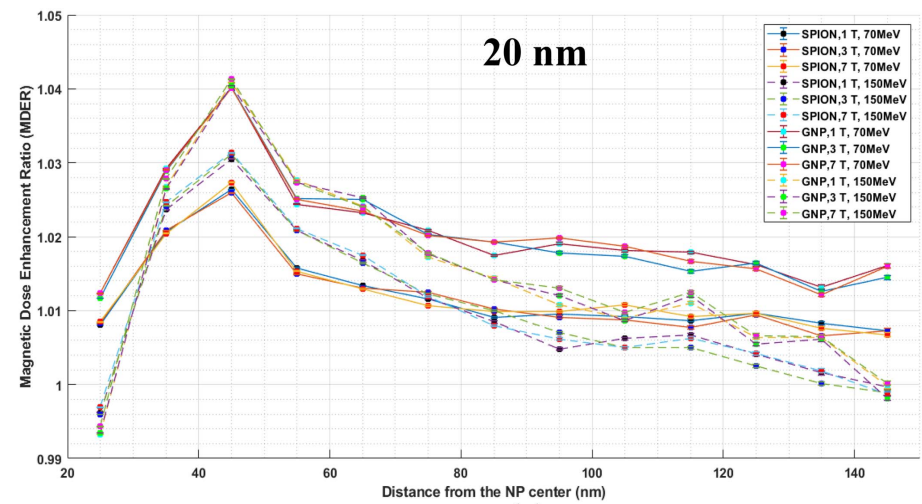
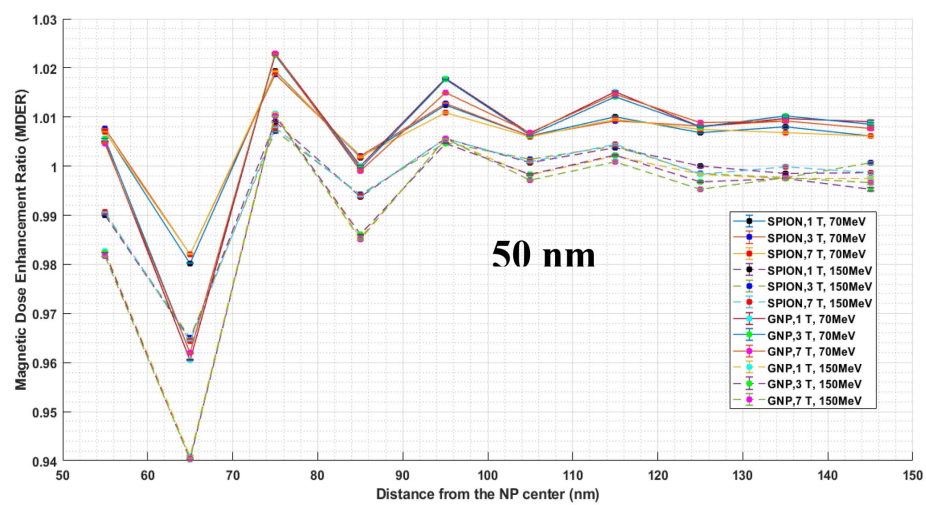


**Figure 5.** Left column: the dose distribution of the secondary electrons produced in the interaction of 70 and 150 MeV primary proton beams with 50 nm radii NPs in different magnetic field strengths. Dose values were normalized to the total number of primary protons in the run. Right column: Dose enhancement ratios (DER) resulted from ratios of curves in their left figures.

NP is observable, especially for 20 nm NPs (figure 6). Figure 7(a) shows the accumulated dose,  $\text{Dose}_{500 \text{ nm}}$ , within the 500 nm thickness of a spherical shell started from the surface of the NPs. In this distance, the difference between the surrounding scoring volume for 20 nm and 50 nm radius NP is negligible, so the dose can be compared more accurately. As expected, the total dose for NP with higher atomic number and also for 70 MeV beam is higher, that is clear in the comparison between a 50 nm GNP in the 70 MeV beam and other cases.  $\text{DER}_{500 \text{ nm}}$  is shown in figure 7(b), whose values are up to 10 and 4 in the 70 MeV beam for GNP and

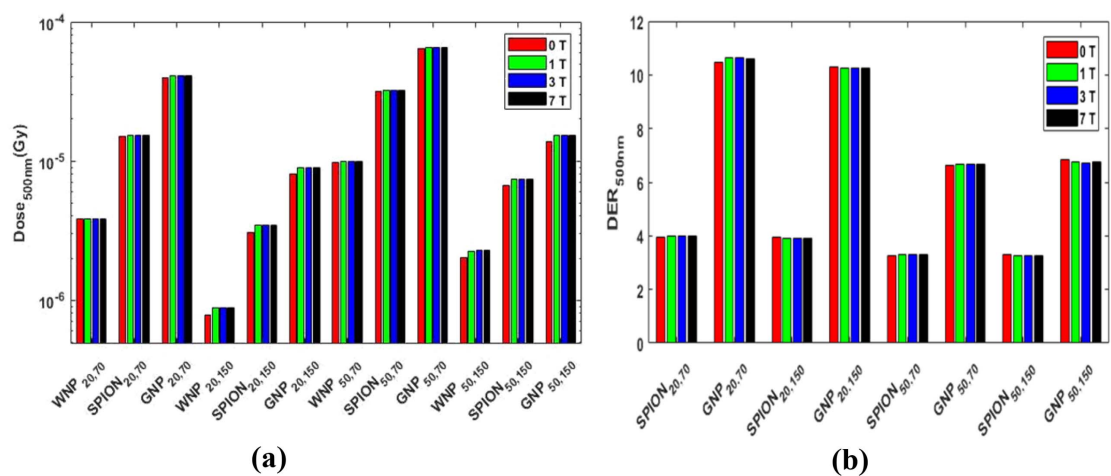


(a)



(b)

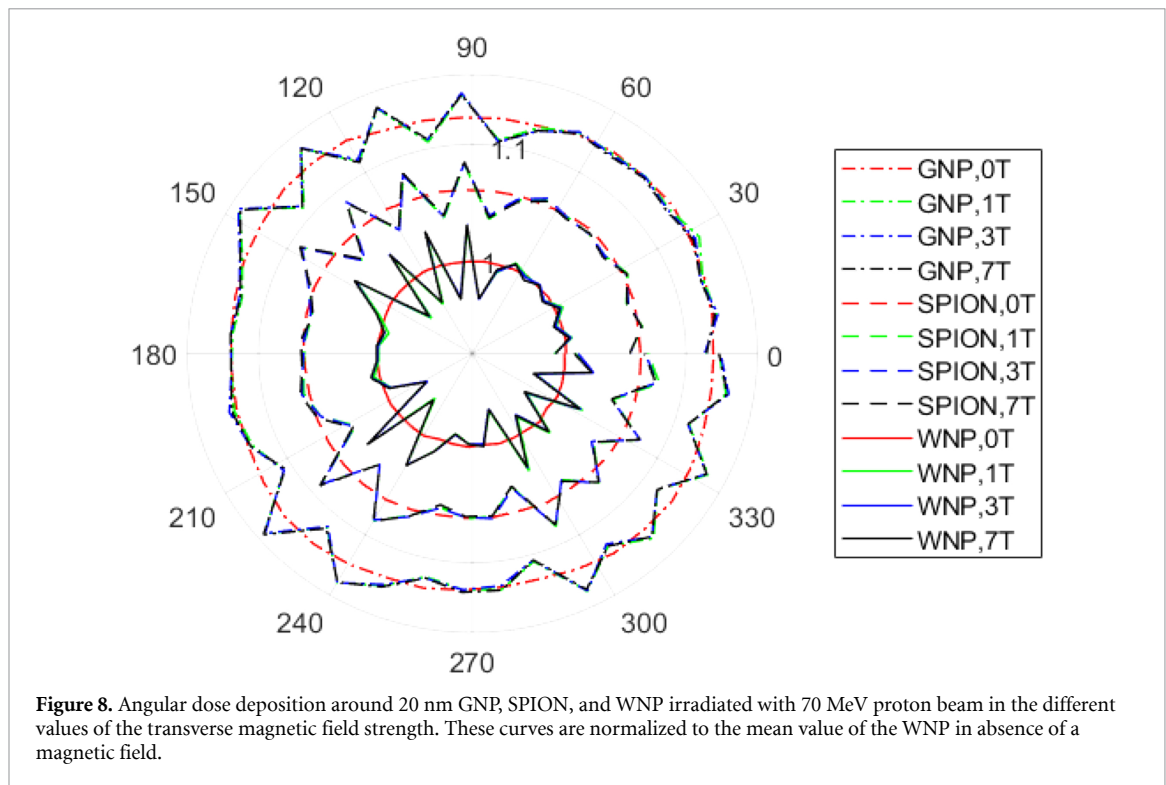
**Figure 6.** Magnetic dose enhancement ratio (MDER) for 20 nm (a) and 50 nm (b) radius NPs. MDER is the ratio of the DER in the desired MF strength to DER without MF. Error bars are too small and cannot be seen on the data points.



(a)

(b)

**Figure 7.** Dose distribution (a) and DER (b) resulted from secondary electrons liberated from the 20 and 50 nm radii NPs in the 70 and 150 MeV proton beams measured in a 500 nm shell thickness. In a  $X_{a,b}$  symbol, 'X' is the type of NP (WNP, SPION, or GNP), 'a' is NP radius (20 or 50 nm), and 'b' is the proton beam energy (70 or 150 MeV). Dose values were normalized to the total number of primary protons in the run.



SPION, respectively. In these two figures that show further distances from the NPs, there is not a distinguishable difference between various used MF strengths.

The results of angular variation in the dose distribution around NPs are illustrated in figure 8. Based on the Lorentz force, the angle between the MF and direction of electron velocity can change the trajectory of the electron. The presence of an MF caused some fluctuations in the angular dose deposition, but the amplitude of this variation is less than 5% for all of the NPs. The MF strength escalation does not affect this parameter. The isotropic distribution of the dose around WNP in the 0 T MF is not degraded significantly in the SPION and GNP. Also, a considerable variation in the angular distribution of dose was not observed in higher values of the MF. The small fluctuations in the angular dose distribution may result from the intrinsic anisotropic electron liberation from the GNP in the forward direction of the interaction with projectile particles.

The dose of the secondary electrons in the 2 nm thickness central plane of NPs is depicted in figure 9. As can be seen, dose values for GNP are more than SPION and WNP. There is not any considerable difference between the dose values of the same NP in the different MFs.

As shown the secondary produced electrons resulting from the interaction of proton particles with NPs have very low energy, so they rapidly slowdown in water medium before having enough time to experience a curved path in an MF and return more energy to the regions near the interface. However, if the simulations are performed considering air instead of water around NP, i.e. simulation of tumors containing NPs in the lung, the electron return effect may be considerable. Cross-sections for electrons in the air are smaller than water so, through the lower probability of interaction, there is a chance to increase the dose near the interfaces by return of low energy secondary electrons. Only a small number the research was dedicated to the measurement of the electron return effect in a proton beam. An experimentally measured dose at a PMMA-air interface in the different energy of a proton beam showed a small enhancement in the higher MF strengths, but their effects are for distances more than micrometres from the interfaces (Lühr *et al* 2019). Radiobiological effects of NPs in proton radiotherapy can be expected only in a nanometer distance to their surfaces where a large number of produced secondary electrons increase the probability of interaction with critical structures of cells around them (Lin *et al* 2014). Therefore, the importance of micro- and nanoscale dose enhancement investigation is vital in the vicinity of an NP in the presence of an MF. The effect of a perpendicular static MF on the nanodosimetric parameter in a DNA volume was investigated by a group, and no significant impact on the track structure was observed (Lazarakis *et al* 2012). In this simulation study, we showed that DER was not significantly affected by an MF, at least in the first 500 nm distance from the surface of the NPs. Finally, it is worthy to address some limitations in our study. An NP-water interface in a nanoscale range was considered to show the effect of an MF, while this phenomenon is more pronounced in the NP-air interfaces. For the future work, we plan to consider a bulk simulation of NPs with different



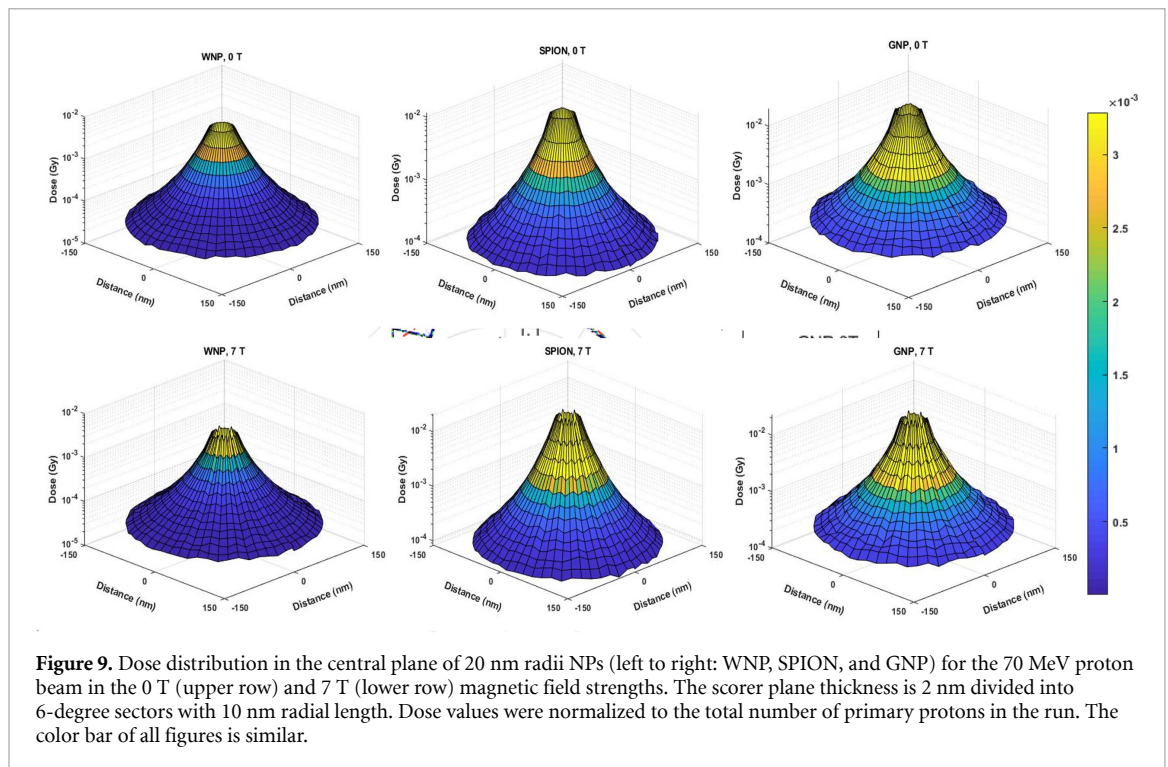


**Figure 9.** Dose distribution in the central plane of 20 nm radii NPs (left to right: WNP, SPION, and GNP) for the 70 MeV proton beam in the 0 T (upper row) and 7 T (lower row) magnetic field strengths. The scorer plane thickness is 2 nm divided into 6-degree sectors with 10 nm radial length. Dose values were normalized to the total number of primary protons in the run. The color bar of all figures is similar.

concentration instead of a singular NP. In this way, the effective atomic number and density of the equivalent combination of the tumor and NPs might be slightly changed. So, on a macroscopic scale, the probability of some phenomena such as ERE will be increased in the interface of the tumor containing NPs and air (tumor-air interface such as the cases in non-small lung cancer). At least, the results of this study are valid until the distance between adjacent NPs is more than considered distance values, 150 and 500 nm, for dose scoring. These distance values, 150 and 500 nm, are equivalent to the uniform distribution of NPs in the water medium with concentrations of about 193 and 5 mg Au g<sup>-1</sup> water for 20 nm radius, 80 and 3540 mg Au g<sup>-1</sup> water for 50 nm radius of GNPs, respectively. The concentration of 20 mg Au g<sup>-1</sup> water has been achieved *in vivo* (Hainfeld *et al* 2004, 2013). This concentration is equivalent to 320 and 800 nm distance between 20 and 50 nm radii of GNPs in a uniform distribution, respectively. So, the assumed singular NP is not far from the experimental situation. However, we should notice that the NPs form clusters in the tumor instead of a uniform distribution (Rahman *et al* 2009). The clustering of NPs might affect the magnetic field strength between themselves, thus the trajectory of primary and secondary charge particles will be changed, that is a macroscopic scale issue and postponed until future studies.

In this study, we just simulated a proton beam though this can be done for photon therapy where DER is several times higher. Thus, a small variation in the directions and trajectories of the emitted secondary electrons influences the manner of energy deposition in the surrounding medium. The measurement of the track length between two consecutive interactions and effective track length and effective range of the secondary electron in a magnetic field as a function of their energy and magnetic field strength could reveal any alteration in electron trajectory (Ahn *et al* 2017). We just consider the probability of dose modification up to 500 nm distances around the NP, but it may be more considerable in further distances due to the presence of the higher energetic electron in the emitted spectrum.

#### 4. Conclusion

In this study, the effects of an MF with different strengths on the dose enhancement ratio in the vicinity of the two types of NPs; GNP and SPION were simulated. Based on the acquired results, the number of liberated secondary electrons and distributed dose to a radius of 500 nm in the water medium surrounding NPs, was not affected significantly. This study showed that the potential of NPs such as GNP or SPION as dose enhancement agents in the proton therapy does not change in an MF, so they can be used in the image-guided proton therapy systems such as MRI guided proton therapy using MF. Further investigations focusing on the tumor-air interfaces and especially for x-ray therapy beam, will reveal the modification of DER in an MF.



## References

- Agrachev M, Antonello S, Dainese T, Ruzzi M, Zoleo A, Aprà E, Govind N, Fortunelli A, Sementa L and Maran F 2017 Magnetic ordering in gold nanoclusters *ACS Omega* **2** 2607–17
- Ahmad R, Royle G, Lourenço A, Schwarz M, Fracchiolla F and Ricketts K 2016a Investigation into the effects of high-Z nano materials in proton therapy *Phys. Med. Biol.* **61** 4537–50
- Ahmad S B, Sarfehnia A, Paudel M R, Kim A, Hissoiny S, Sahgal A and Keller B 2016b Evaluation of a commercial MRI linac based Monte Carlo dose calculation algorithm with Geant4 *Med. Phys.* **43** 894–907
- Ahn S H, Chung K, Shin J W, Cheon W, Han Y, Park H C and Choi D H 2017 Study on dependence of dose enhancement on cluster morphology of gold nanoparticles in radiation therapy using a body-centred cubic model *Phys. Med. Biol.* **62** 7729–40
- Ahn S H, Lee N, Choi C, Shin S W, Han Y and Park H C 2018 Feasibility study of Fe<sub>3</sub>O<sub>4</sub>/TaO nanoparticles as a radiosensitizer for proton therapy *Phys. Med. Biol.* **63** 114001
- Ashburner J 2009 Computational anatomy with the SPM software *Magn. Reson. Imaging* **27** 1163–74
- Boye D, Lomax T and Knopf A 2013 Mapping motion from 4D-MRI to 3D-CT for use in 4D dose calculations: a technical feasibility study *Med. Phys.* **40** 061702
- Bug M U, Gargioni E, Guatelli S, Incerti S, Rabus H, Schulte R and Rosenfeld A B 2010 Effect of a magnetic field on the track structure of low-energy electrons: a Monte Carlo study *Eur. Phys. J. D* **60** 85–92
- Cho J, Gonzalez-Lepera C, Manohar N, Kerr M, Krishnan S and Cho S H 2016 Quantitative investigation of physical factors contributing to gold nanoparticle-mediated proton dose enhancement *Phys. Med. Biol.* **61** 2562–81
- Chu J C H, Reiffel L, Naqvi S, Li X A, Ye S-J and Saxena A 2000 The use of magnetic fields to improve photon dose distributions for radiation therapy—a possible approach to ‘poor man’s proton’ beam properties *Ann. Int. Conf. of the IEEE Engineering in Medicine and Biology Proc.* (Chicago, IL, 23–28 July 2000) (Piscataway, NJ: IEEE) vol 4 pp 2737–40
- De Jong W H, Hagens W I, Krystek P, Burger M C, Sips A J A M and Geertsma R E 2008 Particle size-dependent organ distribution of gold nanoparticles after intravenous administration *Biomaterials* **29** 1912–19
- Francis Z, Incerti S, Karamitros M, Tran H N and Villagrasa C 2011 Stopping power and ranges of electrons, protons and alpha particles in liquid water using the Geant4-DNA package *Nucl. Instrum. Methods Phys. Res. Sect. B Beam Interact. with Mater. Atoms* **269** 2307–11
- Fuchs H, Moser P, Gröschl M and Georg D 2017 Magnetic field effects on particle beams and their implications for dose calculation in MR-guided particle therapy *Med. Phys.* **44** 1149–56
- Geant4-Collaboration 2019 *Physics Reference Manual* (Geneva: CERN)
- Gómez Vitoria M, Weick G, Weinmann D and Jalabert R A 2018 Orbital magnetism in ensembles of gold nanoparticles *Phys. Rev. B* **98** 195417
- Hainfeld J F, Slatkin D N and Smilowitz H M 2004 The use of gold nanoparticles to enhance radiotherapy in mice *Phys. Med. Biol.* **49** N309–15
- Hainfeld J F, Smilowitz H M, O’Connor M J, Dilmanian F A and Slatkin D N 2013 Gold nanoparticle imaging and radiotherapy of brain tumors in mice *Nanomedicine* **8** 1601–9
- Her S, Jaffray D A and Allen C 2017 Gold nanoparticles for applications in cancer radiotherapy: mechanisms and recent advancements *Adv. Drug Deliv. Rev.* **109** 84–101
- Kirkby C and Ghasroddashti E 2015 Targeting mitochondria in cancer cells using gold nanoparticle-enhanced radiotherapy: a Monte Carlo study *Med. Phys.* **42** 1119
- Lacombe S, Porcel E and Scifoni E 2017 Particle therapy and nanomedicine: state of art and research perspectives *Cancer Nanotechnol.* **8** 9
- Lazarakis P, Bug M U, Gargioni E, Guatelli S, Rabus H and Rosenfeld A B 2012 Comparison of nanodosimetric parameters of track structure calculated by the Monte Carlo codes Geant4-DNA and PTra *Phys. Med. Biol.* **57** 1231–50
- Lin Y, McMahon S J, Scarpelli M, Paganetti H and Schuemann J 2014 Comparing gold nano-particle enhanced radiotherapy with protons, megavoltage photons and kilovoltage photons: a Monte Carlo simulation *Phys. Med. Biol.* **59** 7675–89
- Lühr A, Burigo L N, Gantz S, Schellhammer S M and Hoffmann A L 2019 Proton beam electron return effect: Monte Carlo simulations and experimental verification *Phys. Med. Biol.* **64** 035012
- Mckinnon S, Guatelli S, Incerti S, Ivanchenko V, Konstantinov K, Corde S, Lerch M, Tehei M and Rosenfeld A 2016 Local dose enhancement of proton therapy by ceramic oxide nanoparticles investigated with Geant4 simulations *Phys. Medica* **32** 1584–93
- McMahon S J et al 2011a Biological consequences of nanoscale energy deposition near irradiated heavy atom nanoparticles *Sci. Rep.* **1** 1–10
- McMahon S J et al 2011b Nanodosimetric effects of gold nanoparticles in megavoltage radiation therapy *Radiother. Oncol.* **100** 412–6
- McMahon S J, Paganetti H and Prise K M 2016 Optimising element choice for nanoparticle radiosensitisers *Nanoscale* **8** 581–9
- Moteabbed M, Schuemann J and Paganetti H 2014 Dosimetric feasibility of real-time MRI-guided proton therapy *Med. Phys.* **41** 111713
- Nikjoo H, Uehara S and Emfietzoglou D 2012 *Interaction of Radiation with Matter* (Boca Raton, FL: CRC press)
- Ortega R A and Giorgio T D 2012 A mathematical model of superparamagnetic iron oxide nanoparticle magnetic behavior to guide the design of novel nanomaterials *J. Nanoparticle Res.* **14** 1282
- Paganelli C et al 2018 MRI-guidance for motion management in external beam radiotherapy: current status and future challenges *Phys. Med. Biol.* **63** 22TR03
- Perl J, Shin J, Schümann J, Faddegon B and Paganetti H 2012 TOPAS: an innovative proton Monte Carlo platform for research and clinical applications *Med. Phys.* **39** 6818–37
- Popovtzer A, Mizrahi A, Motiei M, Bragilovski D, Lubimov L, Levi M, Hilly O, Ben-Aharon I and Popovtzer R 2016 Actively targeted gold nanoparticles as novel radiosensitizer agents: an *in vivo* head and neck cancer model *Nanoscale* **8** 2678–85
- Raaijmakers A J E, Raaijmakers B W and Lagendijk J J W 2008 Magnetic-field-induced dose effects in MR-guided radiotherapy systems: dependence on the magnetic field strength *Phys. Med. Biol.* **53** 909–23
- Raaijmakers B W, Raaijmakers A J E and Lagendijk J J W 2008 Feasibility of MRI guided proton therapy: magnetic field dose effects *Phys. Med. Biol.* **53** 5615
- Rahman W N, Bishara N, Ackerly T, He C F, Jackson P, Wong C, Davidson R and Geso M 2009 Enhancement of radiation effects by gold nanoparticles for superficial radiation therapy *Nanomed. Nanotechnol., Biol. Med.* **5** 136–42
- Schellhammer S M, Hoffmann A L, Gantz S, Smeets J, van der Kraaij E, Quets S, Pieck S, Karsch L and Pawelke J 2018 Integrating a low-field open MR scanner with a static proton research beam line: proof of concept *Phys. Med. Biol.* **63** 23LT01

- Sotiropoulos M, Henthorn N T, Warmenhoven J W, Mackay R I, Kirkby K J and Merchant M J 2017 Modelling direct DNA damage for gold nanoparticle enhanced proton therapy *Nanoscale* **9** 18413–22
- Stemkens B, Paulson E S and Tijssen R H N 2018 Nuts and bolts of 4D-MRI for radiotherapy *Phys. Med. Biol.* **63** 21TR01
- Stemkens B, Prins F M, Bruijnen T, Kerkmeijer L G W, Lagendijk J J W, van den Berg C A T and Tijssen R H N 2019 A dual-purpose MRI acquisition to combine 4D-MRI and dynamic contrast-enhanced imaging for abdominal radiotherapy planning *Phys. Med. Biol.* **64** 06NT02
- Tran H N *et al* 2016 Geant4 Monte Carlo simulation of absorbed dose and radiolysis yields enhancement from a gold nanoparticle under MeV proton irradiation *Nucl. Instrum. Methods Phys. Res. Sect. B Beam Interact. with Mater. Atoms* **373** 126–39
- Usami N, Furusawa Y, Kobayashi K, Lacombe S, Reynaud-Angelin A, Sage E, Wu T-D, Croisy A, Guerquin-Kern J-L and Le Sech C 2008 Mammalian cells loaded with platinum-containing molecules are sensitized to fast atomic ions *Int. J. Radiat. Biol.* **84** 603–11
- Uz M, Bulmus V and Alsoy Altinkaya S 2016 Effect of PEG grafting density and hydrodynamic volume on gold nanoparticle-cell interactions: an investigation on cell cycle, apoptosis, and DNA damage *Langmuir* **32** 5997–6009
- Wälzlein C, Scifoni E, Krämer M and Durante M 2014 Simulations of dose enhancement for heavy atom nanoparticles irradiated by protons *Phys. Med. Biol.* **59** 1441–58